Supporting Information

# Revealing the Dynamical Role of Co-Solvents in the Coupled Folding and Dimerization of Insulin

*Xin-Xing Zhang* and Andrei Tokmakoff**

Department of Chemistry, James Franck Institute, and Institute for Biophysical Dynamics,

University of Chicago

929 E. 57th St., Chicago, IL 60637, United States

## Outline

10. Effect of Co-Solvents on the Insulin Structure and Dissociation Kinetics

## 1. Methods and Materials

### Sample preparation

Recombinant human insulin (PDB code: 3W7Y) was purchased from Sigma-Aldrich and used without further purification. All measurements were taken in a solution containing 10% (v./v) dimethyl sulfoxide (DMSO), 100 mM NaCl 20 mM Tris and 270 mM HCl, pH 0.5 verified with a pH meter. For IR spectroscopy, these samples were H/D exchanged by dissolving in $D_2O$ at ~1 mg/mL, heating at 65 °C for 30 mins, and lyophilized. Unless specified, the concentration of insulin used in the measurements was 10 mg/mL (1.7 mM). DMSO was purchased from Fisher Scientific. Deuterated solvents used in IR measurements were from Cambridge Isotope Laboratories.

### Circular dichroism spectroscopy

The temperature-dependent ellipticity $\theta$ was measured using a Jasco J-1500 spectropolarimeter. To avoid the detector saturation, Hellma quartz cuvette with path length 10μm and 1 mm are used for measuring $\theta$ at 222nm and 276nm, respectively.

### Isothermal titration calorimetry

Isothermal titration calorimetry (ITC) measurements were carried out using a Microcal iTC200 system. For each titration, an insulin solution with a concentration between 2-4 mM was loaded in a stirring syringe and injected in precisely known aliquots into solution held in the calorimetric cell while a sensor records the time-dependent input of power required to re-equilibrate the system through dimer dissociation. Injections were repeated at equal time intervals of 150 s, while stirring at 1000 rpm. All solutions were degassed before use.

### Temperature ramp FTIR spectra

Our analysis of IR absorption spectra centers on amide I carbonyl vibrations of the polypeptide backbone. For all experiments, the sample was held between two $CaF_2$ windows separated by a 50 μm Teflon spacer, held in a temperature-regulated brass jacket. Temperature-dependent IR spectra were acquired using a Bruker Tensor 27 Fourier-transform infrared (FTIR) spectrometer by acquiring a series of spectra during a slow temperature-ramp from 20 to 90 °C in 2 °C steps with a 60 s equilibration time between spectra. The sample temperature was monitored with a Phidget K-type thermocouple attached to the brass jacket. Data were rejected if any aggregation peak at

1615-1625 $cm^{-1}$ was observed.

### Nonlinear IR spectroscopy

The instrumentation and methods for acquiring steady-state and transient nonlinear IR data have been described previously.[1] Briefly, experiments are performed in the boxcar geometry with three variably time-delayed pulses generating the nonlinear signal and a fourth reference pulse used for balanced heterodyne spectral interferometry. For 2D IR spectra, the nonlinear signal was collected at a fixed waiting time $\tau_2$ = 150 fs as a function of evolution time $\tau_1$ scanned in 4 fs steps out to 2500 and 2000 fs for rephasing and non-rephasing spectra, respectively. The t-HDVE (transient heterodyned dispersed vibrational echo) data were collected over a time window from 5 ns to 50 ms after a 15 $^oC$ T-jump. To extend the observation time window, which is limited by the thermal re-equilibration time of solvent, we coated the $CaF_2$ windows with 12.5 μm Dupont FEP fluorocarbon film using vacuum oven (Fisherbrand Isotemp Model 281A). Optical quality coating was achieved by heating the film attached windows at 290 $^oC$ for 30 mins under vacuum. The t-HDVE spectra were collected using the Fourier transform spectral interferometry method, with the local oscillator stepped from −10 to 10 fs in 5 fs steps.

## 2. Overview of the Insulin Structure

Insulin molecule contains 51 residues with 21 on the A chain and 30 on the B chain. The molecule is linked by three disulfide bridges (two inter-chain A7-B7 and A20-B19, and one intra-chain A6-A11). Among the bridges, A6-A11 is relatively flexible, and A20-B19 presumably stabilizes the entire molecule. A7-B7 restrains the two N-terminals. As summarized in Table S1, the structure of insulin in solutions includes three helices (A2-8, A13-19 and B9-19), two β-turns (B7-10, B20-23) and one β-strand (B24-28).[2] The hydrophobic core of insulin in dimer form is composed of four elements: central helix (B9-19), a mostly buried disulfide bridge (A20-B19) and a β-turn (B20-23) which allows the β-strand to pack. Among the helices, A2-8 is weakly folded. The formation of dimer is predominantly non-polar, with the extended chain at B24-26 formed a sheet. Insulin dimers can transform from R to T state. In R state, B2-B19 forms a long α-helix, whereas B1-B8 is extended into a coil in T state. All solution structures of insulin and its analogs exhibit the T state.[3] The Hydrogen-bond between A7 carbonyl and B5 (Histidine) side chain NH is important for the formation of A7-B7 disulfide bridge.

Mutation studies suggest that B6 (Leucine) and B5 (Histidine) are important in receptor binding by adjusting to proper conformation.[3-4] The binding activity of insulin is also sensitive to the chirality of B8Gly, where D-substitution enhances the stability but impairs the receptor binding and L-substitution has the opposite effect.[5-6] B24 phenylalanine to glycine substitution shows that B24 plays a key role in the structural switch from "closed" to "open" state in which the buried residues A2A3 are exposed to enable the key residues of the receptor to bind them.[6]

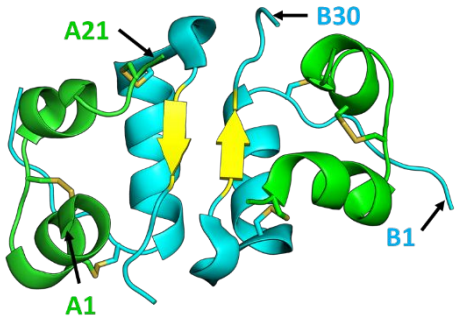


**Figure S1.** Illustration of insulin dimer (PDB: 3W7Y) with A and B chains shown in green and cyan, respectively. Yellow arrows indicate the position of $Phe^{B24, B25}$ at the dimer interface. Disulfide bridges are presented in gold lines. The N- and C-terminus of the two chains are pointed out with arrows.

**Table S1.** Structural Details of Insulin Dimer in Solution

| Species | Residues |
|---|---|
| α-helix | A2-8, A13-19, B9-19 |
| β-strand | B24-28 |
| β-turn | B7-10, B20-23 |
| Interface | B16Tyr, B24Phe and B26Phe with 6 aromatic rings packing |
| Buried Residues | Leu (A16, B6, B11,B15), Cys (A6, A11, B19), A19Tyr, A2Ile, B14Ala |

## 3. Dissociation Parameters Obtained with ITC

The ITC measures the heat required for the solution in the cell to equilibrate during the titration of a concentrated insulin solution at a fixed temperature, as shown in Figure S2a. Thus, no heat contribution is expected from the unfolding process since the equilibrium conformational ensemble associated with the monomer and dimer structures does not vary with concentration. The released heat $q_i$ when the $i^{th}$ injection of volume $\delta V$ is titrated into a cell with an initial volume ($V_0$) of solution can be expressed in terms of the enthalpy of dissociation,

$$q_i = \Delta H_d \left([D]_{syr} - [D]_i\right)\delta V - \Delta H_d \left([D]_i - [D]_{i-1}\right)\left[V_0 + (i-1)\cdot\delta V\right] + q_{off} \tag{S2}$$

Here, $[D]_i$ and $[D]_{syr}$ are dimer concentration in the cell after the $i^{th}$ injection and for the original solution in the syringe, respectively. $q_{off}$ accounts for the calorimeter offset. To fit the curve with eq S1, we need to describe $[D]_i$ with a proper model. In the two-state (dimer-monomer) scenario, the dimer concentration expressed as

$$[D]_i = \frac{[C_{tot}]_i}{2} + \frac{K_d}{8}\left(1 - \sqrt{1 + \frac{8[C_{tot}]_i}{K_d}}\right) \tag{S3}$$

$$[C_{tot}]_i = \frac{C_{syr}\cdot i\cdot\delta V}{V_0 + i\cdot\delta V} \tag{S4}$$

Here, $C_{syr}$ is the equivalent concentration of insulin monomers in the syringe. By inserting eq S2 and S3 into eq S1, and fitting $q_i$ as a function of $[C_{tot}]_i$ for each injection, we obtain the dissociation constants $K_d$ and enthalpy change $\Delta H_d^0$, as illustrated in Figure S2b and c. The obtained parameters at 15, 25 and 35 °C are summarized in Table S2.

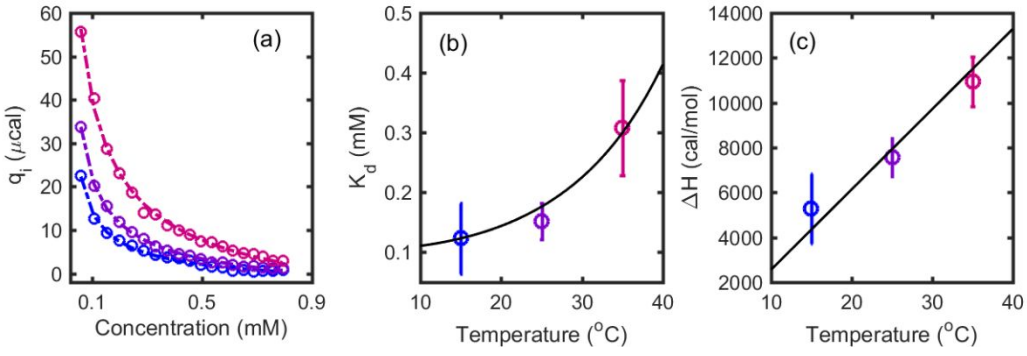

**Figure S2.** (a) ITC titration data (dots) of insulin in 10% DMSO, pH0.5 solution measured at 15 (blue), 25 (purple) and 35 °C (pink) and their fits to eq S1 using two-state model in dashed lines. The obtained (b) dissociation constant $K_d$ and (c) enthalpy change $\Delta H_d$.

**Table S2.** Dissociation Constant and Enthalpy Obtained with ITC using Two-State Analysis*

| $K_d$ ($10^{-4}$ M) | | | $\Delta H_d$ (kcal/mol) | | |
|---|---|---|---|---|---|
| 15 °C | 25 °C | 35 °C | 15 °C | 25 °C | 35 °C |
| 1.23±0.06 | 1.52±0.03 | 3.08±0.08 | 5.3±1.2 | 7.6±0.7 | 10.9±0.9 |

** Two-state analysis is performed using eq S1 and S2.*

## 4. Thermodynamic Analysis of Insulin Dimer-Monomer Transition

A simple two-state model involving an equilibrium between a dimer (D) and two indistinguishable monomers (M) is the most straightforward way to describe the dimer dissociation thermodynamics:

$$D \overset{K_d}{\rightleftarrows} 2M \tag{S5}$$

The dissociation constant and the standard-state free energy of dissociation are related in the usual way: $K_d = [M]^2 / [D] = \exp(-\Delta G_d^0 / RT)$, and the dimer fraction $\alpha_D$ can be expressed in terms of $K_d$ and the total insulin concentration $C_{tot}$=[$M$]+2[$D$],

$$\alpha_D(T) = 1 + \frac{K_d(T) - \sqrt{K_d^2(T) + 8C_{tot}K_d(T)}}{4C_{tot}} \tag{S6}$$

In our analysis, the temperature-dependence of $\Delta G_d^0$ is described by a Gibbs-Helmholtz relation,

$$\Delta G_d^0(T) = \Delta H_d^0 - T\Delta S_d^0 + \Delta C_p^0 \left[ T - T_0 - T\ln\left(\frac{T}{T_0}\right) \right] \tag{S7}$$

in which temperature-dependent changes to the enthalpy and entropy of dissociation are expressed relative to a reference temperature $T_0$ at which $K_d$=1M and $\Delta G_d^0 = 0$.[7-8] $\Delta C_p^0$ is the heat-capacity change on dimer dissociation and is independent of temperature.

To apply this model, the absolute value of $\alpha_D$ at various temperature is required, however IR"(1683) only provides information on changes proportional to $\alpha_D$. To add additional constraints for modeling, ITC was used to obtain the dissociation enthalpy $\Delta H_d$ and dissociation constant $K_d$ for the insulin monomer-dimer equilibrium at three temperatures (Table S2). At a fixed temperature the equilibrium conformational ensemble associated with the monomer and dimer structures does not vary with concentration, meaning the released heat upon titration is correlated only with the enthalpy change of dissociation. As a final constraint on $\alpha_D$, the UV CD measurements of the temperature-dependent molar ellipticity at 276 nm $\theta_{276}$ (Figure 2b) was measured. This is an indicator tracking insulin dimers, due to its sensitivity to the tyrosyl signal caused by interactions at the dimer interface.[9]

A self-consistent analysis of CD, ITC, and IR experiments was applied by using these $K_d$ values from ITC as constraints in relating the IR"(1683) and $\theta_{276}$ to the dimer fraction, with the results shown in Figure 2c. The thermodynamic parameters in eq S6, are first estimated by fitting $K_d$ and $\Delta H_d$ in Table S2, and then used as initial values in fitting the melting curves described by a rescaled IR"(1683) and $\theta_{276}$ in Figure 2c. Considering that a slight variation of $\Delta H_d^0$, $\Delta C_p$ and $T_0$ causes dramatic change in $\alpha_D(T)$, we constrain $K_d$ to be within ±5% of the initial values determined by ITC. The thermodynamic parameters are achieved and listed in Table S3.

Table S3. **Thermodynamic Parameters of Dimer Dissociation at $T_0$ (113.5°C)**

| Process | $\Delta H_i^j$ * (kcal mol$^{-1}$) | $\Delta S_d^j$ (cal mol$^{-1}$K$^{-1}$) | $\Delta C_p^j$ (cal mol$^{-1}$K$^{-1}$) | $k_{0,i}$ |
|---|---|---|---|---|
| equilibrium | 39.6 | 102 | 357 | -- |
| association | 69.8 | 180 | 1050 | $3.51\times10^{10}$ M$^{-1}$s$^{-1}$ |
| dissociation | 109.3 | 282 | 1407 | $3.51\times10^{10}$ s$^{-1}$ |

* j = 0 and †, indicating the equilibrium and transient process, respectively. i = a and d, representing the association and dissociation, respectively.

## 5. Aggregation of Insulin Observed by FTIR and CD Spectra

In general, protein amyloid-like aggregation is rich in intermolecular β-sheet structure, [10] which is usually observed as an irreversible absorption change at ~1620 $cm^{-1}$ in IR spectra. Sneideris et al. have shown that the formation of insulin fibrils can be induced by low pH, co-solvent or sequence modification.[11] Salt concentration also plays an important role in shifting the equilibrium from monomers to oligomers.[12] As illustrated in Figure S3a, with the presence of 10% DMSO and 270 mM hydrochloric acid, the absorption of insulin at 1617 $cm^{-1}$ increases significantly at temperatures above 70 °C, indicating the formation of fibrils. The amyloid-like aggregation enhances the interaction between side chains, thus remarkedly affects the ellipticity at 276 nm $\theta_{276}$, as shown in Figure S3b. Thus, 70 °C is defined as the aggregation temperature, above which the experimental data are excluded in the study of insulin dimer-monomer transition. Similar aggregation temperature of insulin is observed by Dzwolak et al. in water at pH 1.9 using DSC/PPC calorimetry.[13] Their results suggest that the formation of insulin fibrils occurs with endothermic unfolding into bulky intermediates and followed by an irreversible exothermic aggregation.

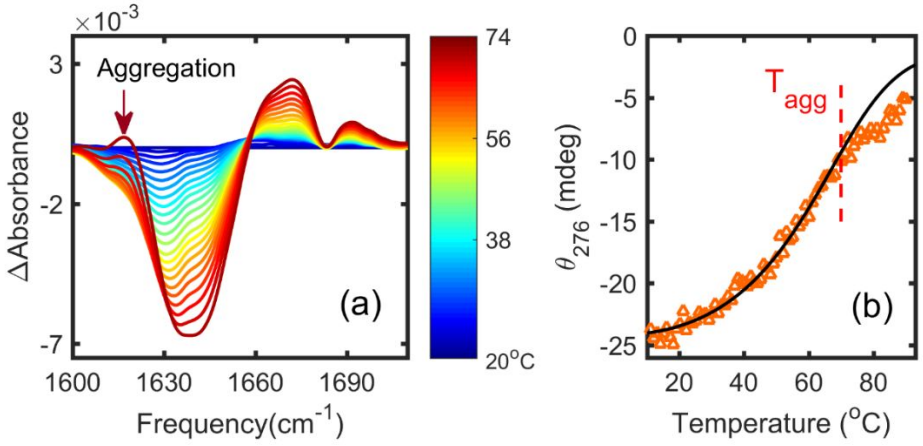


**Figure S3.** Aggregation signal observed with (a) FTIR spectra and (b) ellipticity at 276 nm. Aggregation temperature $T_{agg}$ = 70 °C. is marked with dashed line.

## 6. Thermal-Induced Dissociation Kinetics of Insulin observed by T-jump IR Spectra

Figure S4 compares the time-dependent spectral evolutions at different temperatures. At T-jump delay t = 100ns, an immediate change of intensity across the spectrum is observed as an intensity loss at 1635 $cm^{-1}$, together with a pair of gain features at 1610 and 1660 $cm^{-1}$. Among these features, only the peak intensity at 1660 $cm^{-1}$ displays a strong dependence on the temperature. Given this time scale (100 ns) is too short for significant dissociation to occur but long enough for solvent configuration and short-range motions, we attribute these features to the weakening of H-bonds within the protein and at the dimer interfaces that result from the density change and increased thermal fluctuations.[14] The temperature dependence of 1660 $cm^{-1}$ peak intensity at 100 ns, implies the sensitivity of this frequency to the degree of structural flexibility and water accessibility of insulin molecules. With time delays increasing to several hundred microseconds, the dominant positive peak shifts to 1671 $cm^{-1}$, resulting from the loss of interfacial β-sheet and gain of random structures due to the dimer dissociation. As discussed in the main text, the significant intensity loss centered at 1640 $cm^{-1}$ is caused by the melting of both β-sheet and α-helical structures. In the t-HDVE spectra, both the maximum intensity at 1671 $cm^{-1}$ and the minimum intensity at 1640 $cm^{-1}$, show strong temperature dependence, which is due to the variation of dimer fraction, or for the spectra measured at low T, the insufficient time window that fails to capture the complete dissociation process.

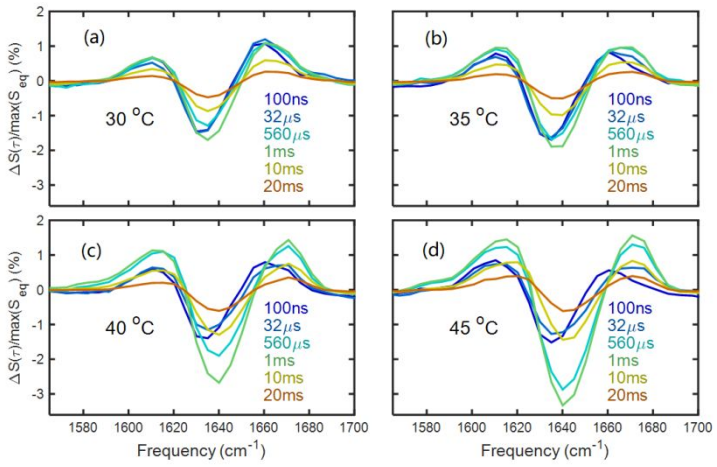


**Figure S4.** Difference t-HDVE spectra as a function of T-jump delay time measured at initial temperature (a) 30 °C, (b) 35 °C, (c) 40 °C, and (d) 45 °C, with a T-jump size ΔT = 15 ± 1.7 °C. Polarization is ZZZZ, and $C_{tot}$ = 10 mg/mL insulin.

Figure S5 further illustrates the relaxation process with time-dependent spectral evolution at different frequencies. To characterize the relaxation behavior at each frequency, the t-HDVE traces are fitted using a combination of four stretched exponential functions,

$$R(t) = \sum_{i=1}^{4} a_i \exp\left[-\left(t/\tau_i\right)^{\beta_i}\right] + C \qquad \text{(S8)}$$

Here C is a constant value, which is used to account for the baseline offset at initial T-jump delays. The first and the last stretched exponential functions, are set to capture the fast response happening before 100 ns $R_{SOL}(t)$ and the slowest response following the temperature re-equilibration $R_{LO}(t)$, respectively. The other two functions are assigned to describe the kinetics occurring in the time range of microseconds to milliseconds, indicated with $R_F(t)$ and $R_S(t)$ as a relatively fast and slow responses.

As shown in Figure S5b, eq S7 provides a good characterization of the relaxation behavior at different frequencies. To illustrate the difference of these relaxation behavior, the fitting curves are normalized at 3ms and plotted in Figure S5c. The spectral evolution at 1645 and 1671 $cm^{-1}$ shows extraordinary agreement with their normalized fitting curves hard to be distinguished in the range of 1μs to 1ms. Expect the time trace at 1660 $cm^{-1}$, the rest all contain a large intensity change in the t-DPP signal appearing in the 0.1 – 1ms time window, that is expected to arise from the melting of the dimer interface. The time traces at both 1660 and 1655 $cm^{-1}$, displays a relaxation behavior spanning the range 1 – 20 μs, suggesting a fast response occurring prior to the melting of interfacial β-sheet.

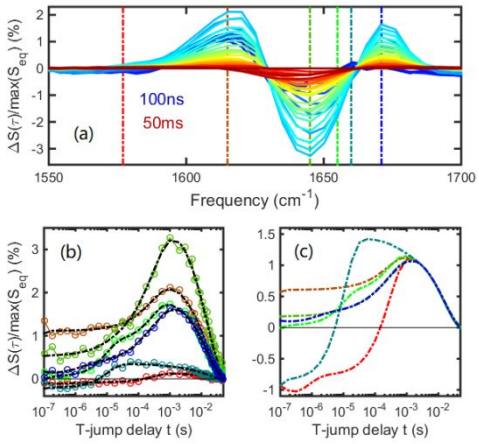


**Figure S5.** Overview of t-HDVE spectra of 10 mg/mL insulin in 10% DMSO, pH 0.5 solution measured at $T_i$ = 50 °C with dT = 14.4 °C, parallel polarization. (a) Difference t-HDVE spectra as

a function of T-jump delay t. (b) Time traces following the spectral evolution at six detection frequencies, which are color-coded with dashed lines at 1577, 1615, 1645, 1655, 1660 and 1671 $cm^{-1}$ in part a. The black dashed lines are the fitting using eq S7. (c) The fitting curves of kinetic traces in b, which are normalized at t = 3 ms.

## 7. Analysis of T-Jump Kinetics and Spectral Component Assignment

For investigating the origin of the fast and slow kinetic responses, the time traces at 1660 and 1671 $cm^{-1}$ are selected to represent $R_F(t)$ and $R_S(t)$, respectively. As discussed earlier, the spectral feature peaked at 1683 $cm^{-1}$ is due to the $\upsilon_P$ vibrational mode of dimer interfacial β-sheet, thus the time-dependent evolution at this frequency serves as a good indicator tracking the dimer dissociation. However, the t-HDVE signal at this frequency is subtle and can be hard to characterize due to the low signal-to-noise ratio. The sum of time traces at 1681 and 1687 $cm^{-1}$ is used instead, for representing the dissociation kinetics and being compared with the spectral evolution at nearby frequencies which have larger signal response. As shown in Figure S6a, the time traces are characterized by fitting them with eq S7, which seem to capture a similar slow relaxation behavior.

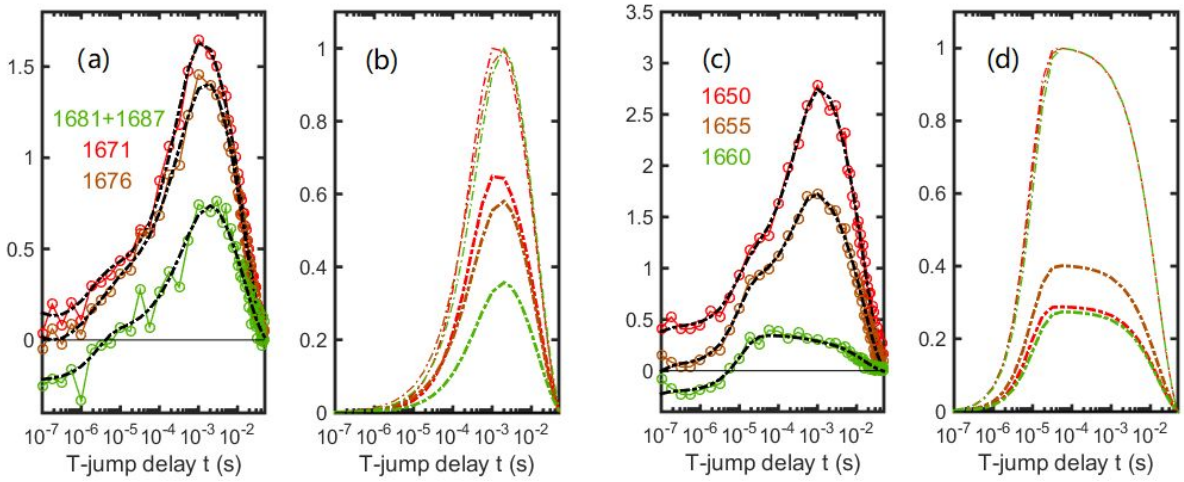


**Figure S6.** Temperature-dependent relaxation kinetics measured at $T_i$ = 50 °C with ΔT = 14.4 °C, parallel polarization. (a) t-DPP amplitude at $\omega_3$ = 1671, 1676, and a sum of amplitude at 1681 and 1687 $cm^{-1}$, and their fitting functions $R_S(t) + R_{LO}(t)$ shown in the same color-coded line. (c) t-DPP amplitude at ω3 = 1650, 1655 and 1660 $cm^{-1}$, and their fitting functions $R_F(t) + R_{LO}(t)$ shown in the same color-coded line. Thinner lines in (b) and (c) are the normalized response functions.

To further test this, this slow kinetic response $K_S(t)$ is represented using a combination of the component $R_S(t)$ and the temperature re-equilibration term $R_{LO}(t)$,

$$K_S(t) = R_S(t) + A_S \cdot R_{LO}(t) \tag{S9}$$

Here, $A_S$ is a scaling factor to ensure $K_S(t)$ is 0 at t = 10 ns. As illustrated in Figure S6b, $Ks(t)$ of the combined time traces at 1681 and 1687 $cm^{-1}$ is nearly indistinguishable from the one at 1676 $cm^{-1}$, whereas slower than that of 1671 $cm^{-1}$. The time-dependent evolution at $\omega_3$ = 1676 $cm^{-1}$, is proved to be consistent with loss of intensity in $\upsilon_P$ β-sheet band arising from the dimer melting, thus can be used as a sensor tracking the dissociation process which is also consistent with our previous study on bovine insulin.[8]

In Figure S6c, the t-HDVE time traces at 1650, 1655 and 1660 $cm^{-1}$, all display a pronounced fast response spanning in the range of 1 – 20 μs. The response $K_F(t)$ is characterized by fitting these time traces with eq S7 and generated by combining the term $R_F(t)$ and $R_{LO}(t)$,

$$K_F(t) = R_F(t) + A_F \cdot R_{LO}(t) \tag{S10}$$

$A_F$ is a scaling factor to ensure $K_S(t)$ is 0 at t = 10 ns. As shown in Figure S6d, the normalized $K_F(t)$ at all frequencies report an identical relaxation behavior.

It is clear that $K_F(t)$ and $K_S(t)$ reflect distinct molecular processes along the dissociation pathway, however, are convolved in the spectral domain. For further interpretation, the CSVD analysis is employed to obtain the spectral components that associate with them. The first three spectral and temporal components in the SVD analysis (whose sum accounts for 72% of the total), are re-weighted by constraining their temporal component to follow $R_S(t)$, $R_F(t)$ and $R_{LO}(t)$. As shown in Figure S7, the spectral component which is constrained to follow the T-jump temperature profile $R_{LO}(t)$, is consistent with the average spectral evolution before 320 ns, thus reflects the spectral changes driven by weakening or disrupting H-bonds fluctuations. The spectral component correlates with $R_S(t)$, has the largest intensity changes in the range of 1660-1690 $cm^{-1}$, consistent with loss of intensity in the $\nu_\perp/\nu_P$ peak band 1635 & 1683 $cm^{-1}$ and gain intensity at 1620 and 1670 $cm^{-1}$ resulting from the spectral broadening due to the random structures. The absence of strong β-sheet loss features in other components indicates that this component captures most of the interfacial β-sheet disruption.

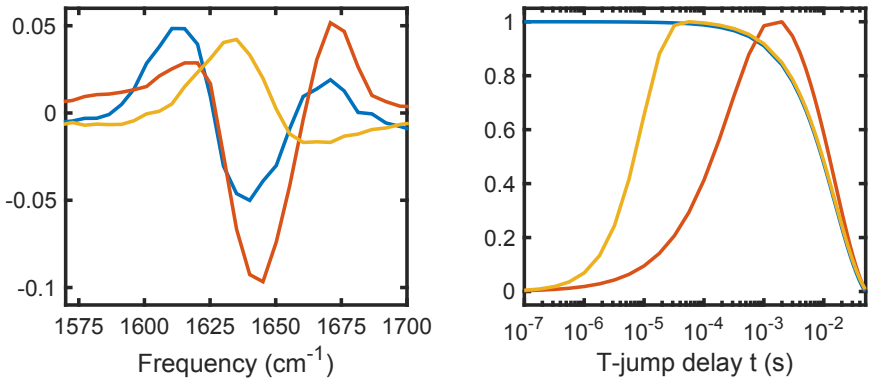


**Figure S7.** CSVD analysis of t-HDVE spectra measured at $T_i$ = 50 °C with ΔT = 14.4 °C, parallel polarization. (left) Spectral component. (right) Temporal component. Components correlated with $R_{SOL}(t)$, $R_F(t)$ and $R_S(t)$ are shown with blue, red and yellow lines, respectively.

The last component associates with $R_F(t)$, displays a gain signal peaked at 1635 cm$^{-1}$ and an intensity loss at 1660 cm$^{-1}$, that are attributed to a transition to a more disordered structure, most likely due to the solvent exposure of buried residues. As shown in Figure S8, both the amplitude and relaxation time varies significantly with the temperature.

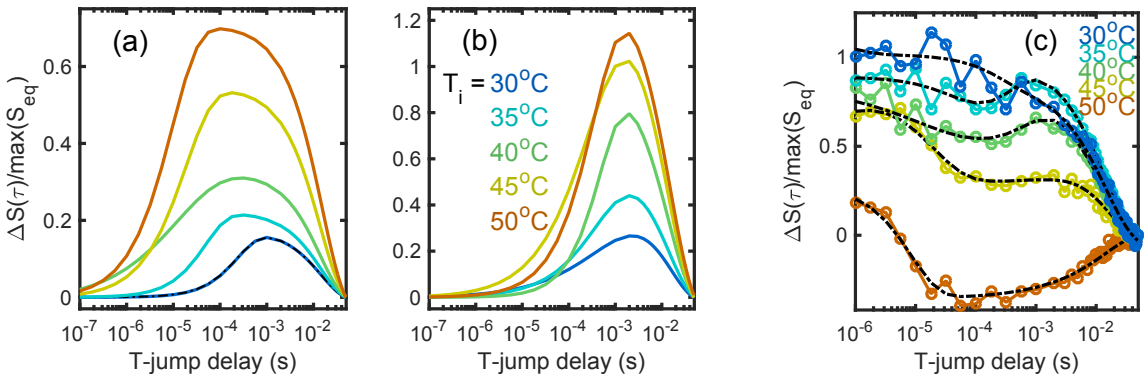


**Figure S8.** Temperature-dependent relaxation kinetics measured various initial temperature with T-jump size 15±1.7 °C, parallel polarization. (a) $K_F(t)$ generated by fitting t-HDVE amplitude at $\omega_3$ = 1660 cm$^{-1}$ using eq S7 and S9. (b) $K_S(t)$ generated by fitting t-HDVE amplitude at $\omega_3$ = 1676 cm$^{-1}$ using eq S7 and S8. (c) t-HDVE time traces at $\omega_3$ = 1660 cm$^{-1}$ and their fitting with eq S7 (dashed line). Due to the low SNR, t-DPP amplitude evolution at 1655 and 1671 cm$^{-1}$ are used instead to represent the fast and slow kinetic response at $T_i$ = 30 °C.

## 8. Comparison of Observed Rates at Various Temperatures

The T-jump relaxation kinetics observed in our experiments, are influenced by the temperature of buffer as it re-equilibrates from $T_f$ to $T_i$. The observed time-dependence of the transient signal S is the convolution of the sample response R and the temperature profile $R_{LO}$,

$$S(t) = R(t) \otimes R_{LO}(t) \tag{S11}$$

Here $R_{LO}(t)$, is characterized by the absorbance change of the local oscillator pulse, which is well fit to a stretched exponential of the form $R_{LO}(t) = \exp\left[-(t/\tau_T)^{\beta}\right]$ where $\tau_T$ and $\beta$ are normally around 13.4 ms and 0.78, respectively. Figure S9a shows examples of simulated T-jump response by convolving an exponential response of the form $\exp(-\lambda_{rise} t)$ with $R_{LO}(t)$ based on Fourier transformation.

$$S(t) = FT^{-1}\left\{FT\left[R(t)\right] \times FT\left[R_{LO}(t)\right]\right\} \tag{S12}$$

To obtain the correlation between the input and observed rate, each convolved signal is fit to a bi-exponential function of the form $-C[\exp(-\lambda_{rise}\tau) - \exp(-\lambda_{decay}\tau)]$. Figure S9b illustrates the mapping between observed rate $\lambda_{rise}$ and the underlying de-convolved rate $\lambda$ based on our kinetic modeling. It is found that $\lambda$ matches $\lambda_{rise}$ when the sample response time is less than 3 ms, and our T-jump experiments fail the detection of any kinetics slower than 11.6 ms.

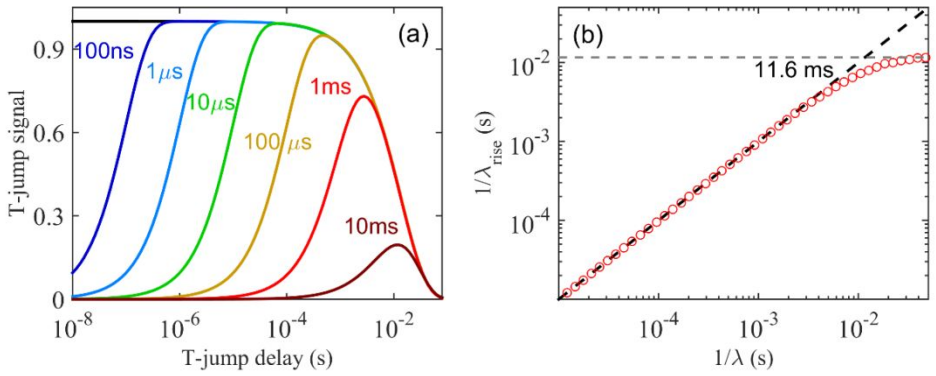

**Figure S9.** Obtained deconvoluted relaxation time from measured experimental rise times. The observed signal that results from convolution (a) is fit to a bi-exponential with a rise time of $1/\lambda_{rise}$. The corresponding deconvoluted relaxation time, $1/\lambda$, is obtained from the blue correlation line (b).

Based on eq S11, temperature-dependent $K_F(t)$ and $K_S(t)$ in Figure S8 are fitted using bi-stretched exponential function. Their average response times are equal to $\beta^{-1}\Gamma\left(\beta^{-1}\right)\lambda_{rise}^{-1}$, and summarized in Table S4 with deviation computed based on 95% confidence interval of fitting. The other method for extracting the average response time, is the maximum entropy method (MEM) analysis which can assist in isolating the temporal and spectral information and provides a smooth rate distribution for the observed kinetics at each detected frequency. Figure S10 illustrates the temperature dependence of the observed dissociation rates. The rates $1/\tau_{MEM}$ are calculated based solely on the purple contour centered at 1671 $cm^{-1}$, with $\tau_{MEM}$ consistently smaller than the corresponding $\tau_S$ listed in Table S4. The correlation between $\tau_{MEM}$ and $\tau_S$ can be described with a linear function,

$$\tau_{MEM}\left(\mu s\right) = 1.45 \times \tau_S\left(\mu s\right) - 332 \tag{S13}$$

The differences between $\tau_{MEM}$ and $\tau_S$ are probably due to the spectral and temporal overlap of the fast and slow kinetic responses.

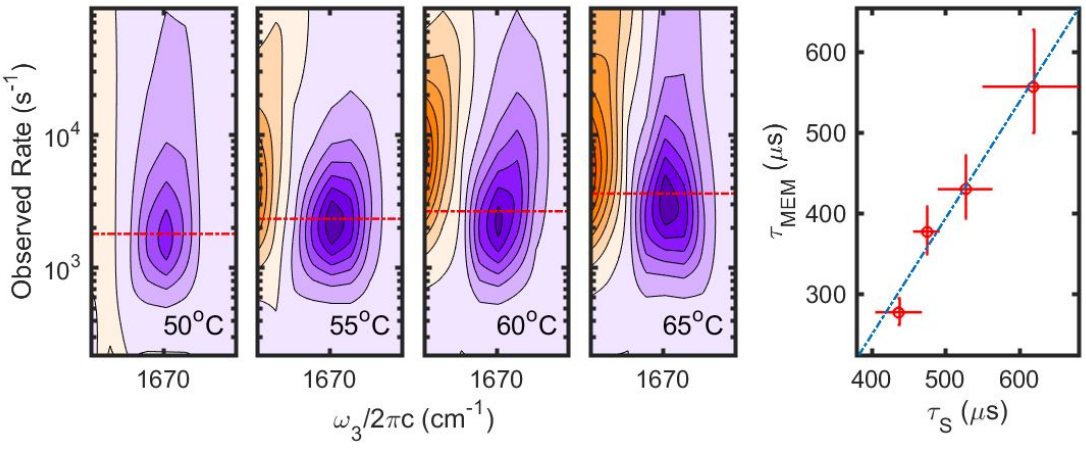


**Figure S10.** (left) MEM rate distributions of t-HDVE data of 10 mg/ml insulin in 10% DMSO, pH0.5 solution measured at final temperature 50, 55, 60 and 65 °C, with ΔT = 15±1.7 °C. Orange and purple contours represent positive and negative rate amplitude, respectively. Dashed lines

indicate the position of average observed rate $1/\tau_{MEM}$ of dissociation process. (right) Comparison of $\tau_{MEM}$ and $\tau_S$ in Table S4. Deviation of $\tau_{MEM}$ is computed with the amplitude-weighted standard deviation of the observed rates across the entirety of the dissociation response. Blue dashed line is generated according to eq S12.

## 9. Analysis of Dimer-Monomer Transition

For investigating the correlation between $R_F(t)$ and $R_S(t)$, the average relaxation time $\tau_F$ and $\tau_S$ are summarized in Table S4, that are obtained by fitting the corresponding CSVD time component with stretch exponential function. As shown in Figure 4a, by increasing the concentration from 10 mg/ml to 30 mg/ml, $\tau_S$ decreases slightly (<20%) at various temperature. For a two-state ($D \rightleftarrows 2M$) transition, the relaxation time has a linear correlation with the total concentration $C_{tot}$,[8]

$$\tau_S^{-2} = k_d^2 + 8k_a k_d C_{tot} = k_d^2 + 8k_d^2 K_d^{-1} C_{tot} \quad \text{(S14)}$$

Here $k_a$ and $k_d$ are association and dissociation rate constants, respectively. $K_d$ can be computed using parameters in Table S3. As a concentration-independent value, $k_d$ calculated with $\tau_{S(10)}$ and $\tau_{S(30)}$ using eq S13 should be consistent. However, the two $k_d$ values differ by 20%-40% at various temperature, informing us that the two-state thermodynamic model overly simplifies the dimer dissociation process by neglecting the accompanied conformational changes during dimer-monomer transition. Studies by CD and NMR indicate that a dissociated monomer has less α-helical structure and a more extended β-strand, compared to the monomer subunit of the dimer [15-16]. Our T-jump measurements suggest that the unfolding process $R_F(t)$ destabilizes the hydrophobic core of dimers thus facilitates the melting of the dimer interface $R_S(t)$. In this scenario, the transition pathway is described as,

$$D \underset{k_f}{\overset{k_u}{\rightleftarrows}} \{D_i\} \underset{k_a}{\overset{k_d}{\rightleftarrows}} M + M \quad \text{(S15)}$$

Here $\{D_i\}$ is the ensemble of dimer intermediate states. The observed rates are given as[7]

$$\tau_F^{-1} = 0.5p + \sqrt{0.25p^2 - q}$$
$$\tau_S^{-1} = 0.5p - \sqrt{0.25p^2 - q}$$
$$p = k_u + k_f + k_d + 4k_a[M] \quad \text{(S16)}$$
$$q = k_u k_d + 4(k_u + k_f)k_a[M]$$

[M] is the monomer concentration at equilibrium. The folding ($k_f$) and unfolding ($k_u$) rate constants characterize the unfolding process of dimer into intermediate states which is not resolvable with equilibrium instruments. Thus, the equilibrium dissociation constant $K_d$ equals $k_d k_a^{-1}$. As discussed earlier, the folding/unfolding process is related with the dimer compaction that appears at a few μs as a solvent exposure signal, while $k_a$ and $k_d$ only describe the formation of dimer interface which is characterized by the loss of interfacial β-sheet distributing at sub-ms timescale. Given the large deviation of $\tau_F$ due to weak T-jump signal, the accuracy of $k_f$ and $k_u$ are much worse than that of $k_d$ and $k_a$. As summarized in Table S4, $k_a$ is 3 magnitudes higher than $k_f$, suggesting a lower free energy barrier of association than that of folding.

**Table S4.** Observed Relaxation Times and Three-State Rate Constants*

| $T_f$ (°C) | $\tau_{F(10)}$ (μs) | $\tau_{S(10)}$ (μs) | $\tau_{S(30)}$ (μs) | $k_f$ ($s^{-1}$) | $k_u$ ($s^{-1}$) | $k_a$ ($M^{-1}s^{-1}$) | $k_d$ ($s^{-1}$) |
|---|---|---|---|---|---|---|---|
| 45 | 260 (±14%) | 1137 (±8%) | 978 (±15%) | $1.13\times10^3$ | $5.69\times10^1$ | $1.22\times10^6$ | $7.18\times10^2$ |
| 50 | 53 (±22%) | 619 (±11%) | 553 (±17%) | $1.68\times10^3$ | $3.89\times10^2$ | $5.14\times10^6$ | $4.52\times10^3$ |
| 55 | 34 (±15%) | 527 (±7%) | 449 (±12%) | $2.50\times10^3$ | $1.90\times10^2$ | $6.37\times10^6$ | $8.47\times10^3$ |
| 60 | 23 (±14%) | 475 (±4%) | 390 (±8%) | $2.99\times10^3$ | $2.58\times10^2$ | $7.32\times10^6$ | $1.53\times10^4$ |
| 65 | 11 (±14%) | 437 (±7%) | 357 (±9%) | $2.91\times10^3$ | $7.01\times10^2$ | $1.13\times10^7$ | $3.82\times10^4$ |

* Deviation of average relaxation time is computed based on 95% confidence intervals. 10 and 30 in the parentheses indicate the total concentration of insulin.

## 10. Diffusion-Limited Rate

To testify the idea that the formation of insulin dimer interface is a diffusion-controlled reaction, we further compare our extracted association rates with predictions using diffusion limited reaction rate theory. At pH 0.5, each insulin monomer carries a charge of $z_M = +6$, and is treated as spherical protein with homogeneously distributed net charge on surface in the calculation,

$$k_a^0 = 8\pi N_A D_M R^* \tag{S17}$$

$$R^* = 2R_M f = \left[ \int_{2R_M}^{\infty} \frac{e^{U/k_B T}}{r^2} dr \right]^{-1} \tag{S18}$$

Here $N_A$ is Avogadro's number, and R* is the critical encounter distance between associating monomers accounting for solvent screening of monomer charges. The Stokes radius of a monomer $R_M$ is 1.19 nm and its diffusion coefficient measured with dynamic light scattering is $D_M = 1.6 \times 10^6$ cm$^2$ s$^{-1}$.[17] U is the Debye-Hückel potential energy, with Debye length 4.27 Å using the dielectric coefficient of 75.8 for the 10% DMSO/$D_2O$ buffer at 25 °C. The calculated diffusion limited association rate is $5.37 \times 10^9$ M$^{-1}$ s$^{-1}$, which is two order of magnitude larger than our observed value is $2.02 \times 10^7$ M$^{-1}$ s$^{-1}$.

## 11. Effect of Co-Solvents on the Insulin Structure and Dissociation Kinetics

CD spectroscopy is commonly used for characterizing the secondary structure of proteins as a function of temperature, salt concentration, pH and co-solvent.[18-19] α-helices have two signature features at 209 and 222 nm, whereas β-strands have one negative CD signal peaked at 216 nm. The α-helix content (%α-helix) can be estimated with the mean residue ellipticity at 222 nm [$\theta_{222}$] using an empirical function,[20]

$$\%\alpha - helix = \left(3000 - \left[\theta_{222}\right]\right) / 39000 \tag{S19}$$

Pocker et al. have studied the mean residue ellipticity change of insulin in water at pH 7 by varying the concentration from 60 nM to 100 μM.[16] By referring to the literature dimer dissociation constant $K_d$, they found that the dimer-monomer transition caused a large change in %α-helix. The %α-helix of native-like dimer and monomer are 45% and 24.2%, respectively.

[$\theta_{222}$] of 10 mg/mL insulin in various solution at pH 0.5 are shown in Figure S11a, and their corresponding %α-helix calculated using eq S18 in Figure S11b. Detector saturation caused by co-solvents for wavelengths under 200 nm affects the S/N ratio. With temperature increasing from 20 °C to $T_{agg}$=70 °C, all solvent conditions result in a monotonic decrease in the ellipticity, due to the increasing monomer fraction and thermal unfolding of both dimers and monomers. [$\theta_{222}$] in 10% DMSO is nearly identical to the one in $H_2O$, suggesting that 10% DMSO causes

negligible influence on the conformation of insulin molecule and the dissociation constant $K_d$. However, 10% EtOH has a notable effect on $[\theta_{222}]$ making the %α-helix drop from 39.5% to 33.7% at 20 °C, as illustrated in Figure S11b. This has previously been noted, but was attributed solely to changes in the monomer-dimer equilibrium.[21] Given that both DMSO and EtOH can destabilize dimers through hydrophobic interaction, this striking difference in %α-helix may be attributed to the denaturation of insulin molecule caused by EtOH. By changing the co-solvent from DMSO to EtOD, the melting of interfacial β-sheet appears at earlier T-jump delay with $\tau_{MEM}$ decreasing from 378 μs to 178 μs as shown with dashed lines in Figure S12. The fast response of insulin is also observed in the 10% EtOD solution, which is centered at 1655 $cm^{-1}$ and $10^5$ $s^{-1}$.

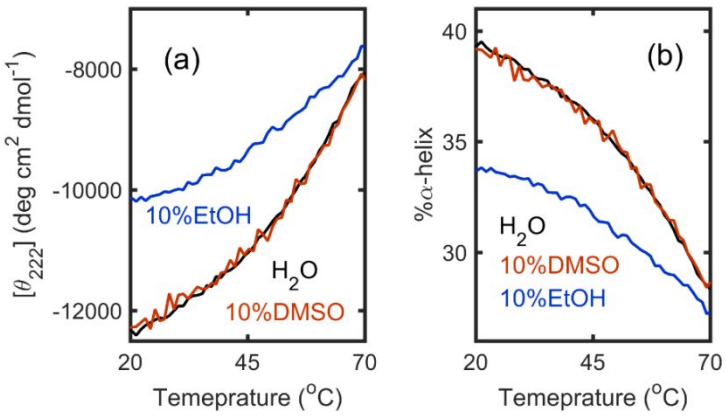

**Figure S11.** (a) Mean residue ellipticity [$\theta_{222}$] of 10 mg/mL insulin in pH 0.5 solution with 20 mM Tris, 100 mM NaCl. Data are the average of at least 3 runs of the same sample. Curves of insulin in 10% EtOH and 10% DMSO have more noise due to the strong UV absorption of EtOH and DMSO. (b) The α-helix content of insulin computed with [$\theta_{222}$] in (a) using eq S18.

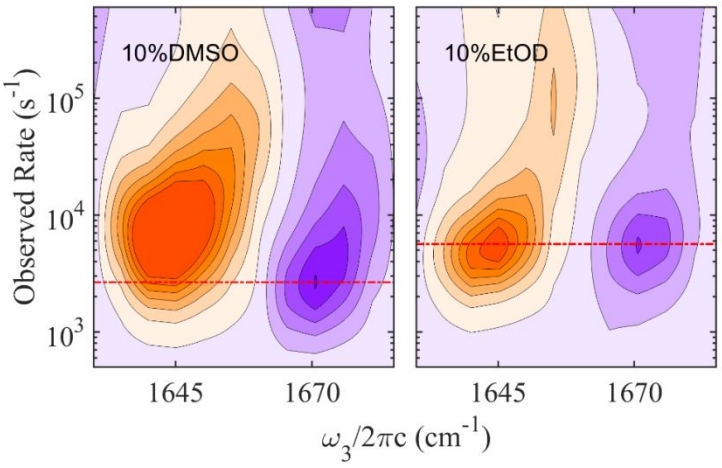


**Figure S12.** MEM rate distributions of t-HDVE data of 10 mg/ml insulin in pH0.5 solution measured at final temperature 60 °C with (left) 10% DMSO and (right) 10% EtOD. Orange and purple contours represent positive and negative rate amplitude, respectively. Amplitudes are rescaled with a time-dependent factor $(1/t)^{0.3}$, for better viewing the weaker signal changes at early T-jump delays. Dashed lines indicate the position of average observed rate $1/\tau_{MEM}$ of dissociation process.

As shown in Figure S13c, the fast response is absent in $D_2O$ solution, confirming its origin of co-solvent effect. The kinetic trace at 1620 cm$^{-1}$, which tracks the ESA change and represents the global structural variation, are compared in Figure S13d. The intensity of 1620 cm$^{-1}$ approaches to its maximum at ~3 ms in water and ~1ms in 10% DMSO, indicating a much slower dissociation kinetics in the absence of co-solvent.

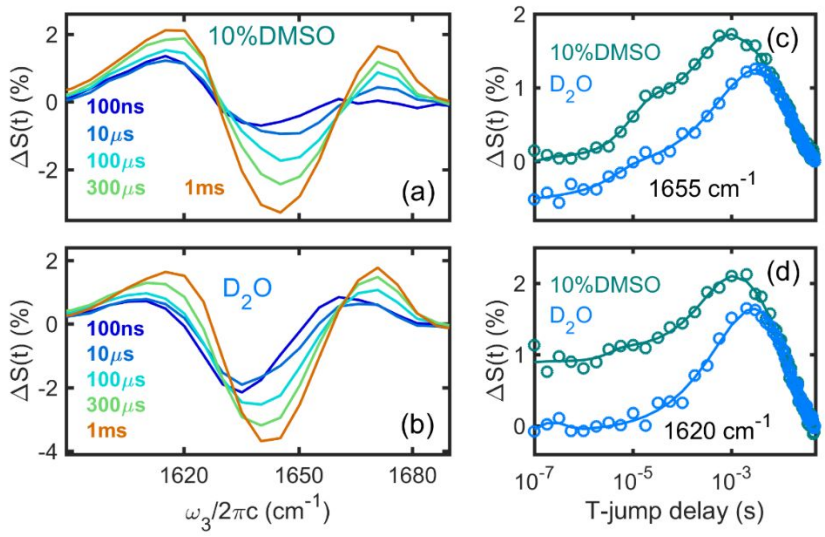


**Figure S13.** Dissociation kinetics of 10 mg/ml insulin observed with T-jump experiments measured at $T_i$ = 50 °C with $\Delta T$ = 15 °C. Representative t-HDVE spectra at select delays in (a)10% DMSO, pH 0.5 solution and (b)$D_2O$, pH 0.5 solution. Comparison of single-frequency kinetic traces representing the dissociation at (c) 1655 $cm^{-1}$ and (d) 1620 $cm^{-1}$ and their fits to eq S7.

## References


1. Sanstead, P. J.; Stevenson, P.; Tokmakoff, A., Sequence-Dependent Mechanism of DNA Oligonucleotide Dehybridization Resolved through Infrared Spectroscopy. *J. Am. Chem. Soc.* **2016**, *138*, 11792-11801.

2. Baker, E. N., et al., The Structure of 2zn Pig Insulin Crystals at 1.5 a Resolution. *Philos. Trans. R. Soc. Lond. B Biol. Sci.* **1988**, *319*, 369-456.

3. Hua, Q., Insulin: A Small Protein with a Long Journey. *Protein Cell* **2010**, *1*, 537-51.

4. Nakagawa, S. H.; Tager, H. S., Implications of Invariant Residue Leub6 in Insulin-Receptor Interactions. *J. Biol. Chem.* **1991**, *266*, 11502-9.

5. Nakagawa, S. H.; Zhao, M.; Hua, Q. X.; Hu, S. Q.; Wan, Z. L.; Jia, W.; Weiss, M. A., Chiral Mutagenesis of Insulin. Foldability and Function Are Inversely Regulated by a Stereospecific Switch in the B Chain. *Biochemistry* **2005**, *44*, 4984-99.

6. Hua, Q. X.; Mayer, J. P.; Jia, W. H.; Zhang, J. W.; Weiss, M. A., The Folding Nucleus of the Insulin Superfamily - a Flexible Peptide Model Foreshadows the Native State. *J. Biol. Chem.* **2006**, *281*, 28131-28142.

7. Noelting, B., *Protein Folding Kinetics*; Spring: Germany, 2006.

8. Zhang, X. X.; Jones, K. C.; Fitzpatrick, A.; Peng, C. S.; Feng, C. J.; Baiz, C. R.; Tokmakoff, A., Studying Protein-Protein Binding through T-Jump Induced Dissociation: Transient 2d Ir Spectroscopy of Insulin Dimer. *J. Phys. Chem. B* **2016**, *120*, 5134-45.

9. Huus, K.; Havelund, S.; Olsen, H. B.; van de Weert, M.; Frokjaer, S., Thermal Dissociation and Unfolding of Insulin. *Biochemistry* **2005**, *44*, 11171-11177.

10. Fitzpatrick, A. W., et al., Atomic Structure and Hierarchical Assembly of a Cross-Beta Amyloid Fibril. *Proc. Natl. Acad. Sci. USA* **2013**, *110*, 5468-73.

11. Sneideris, T.; Darguzis, D.; Botyriute, A.; Grigaliunas, M.; Winter, R.; Smirnovas, V., Ph-Driven Polymorphism of Insulin Amyloid-Like Fibrils. *PLoS One* **2015**, *10*, e0136602.

12. Ziaunys, M.; Sneideris, T.; Smirnovas, V., Self-Inhibition of Insulin Amyloid-Like Aggregation. *Phys. Chem. Chem. Phys.* **2018**, *20*, 27638-27645.

13. Dzwolak, W.; Ravindra, R.; Lendermann, J.; Winter, R., Aggregation of Bovine Insulin Probed by Dsc/Ppc Calorimetry and Ftir Spectroscopy. *Biochemistry* **2003**, *42*, 11347-55.

14. Amunson, K. E.; Kubelka, J., On the Temperature Dependence of Amide I Frequencies of Peptides in Solution. *J. Phys. Chem. B* **2007**, *111*, 9993-8.

15. Roy, M.; Lee, R. W.; Brange, J.; Dunn, M. F., 1h Nmr Spectrum of the Native Human Insulin Monomer. Evidence for Conformational Differences between the Monomer and Aggregated Forms. *J. Biol. Chem.* **1990**, *265*, 5448-52.

16. Pocker, Y.; Biswas, S. B., Conformational Dynamics of Insulin in Solution. Circular Dichroic Studies. *Biochemistry* **1980**, *19*, 5043-9.

17. Oliva, A.; Farina, J.; Llabres, M., Development of Two High-Performance Liquid Chromatographic Methods for the Analysis and Characterization of Insulin and Its Degradation Products in Pharmaceutical Preparations. *J. Chromatogr. B Biomed. Sci. Appl.* **2000**, *749*, 25-34.

18. Greenfield, N. J., Using Circular Dichroism Spectra to Estimate Protein Secondary Structure. *Nat. Protoc.* **2006**, *1*, 2876-90.

19. Kelly, S. M.; Price, N. C., The Use of Circular Dichroism in the Investigation of Protein Structure and Function. *Curr. Protein Pept. Sci.* **2000**, *1*, 349-84.

20. Morrow, J. A.; Segall, M. L.; Lund-Katz, S.; Phillips, M. C.; Knapp, M.; Rupp, B.; Weisgraber, K. H., Differences in Stability among the Human Apolipoprotein E Isoforms Determined by the Amino-Terminal Domain. *Biochemistry* **2000**, *39*, 11657-66.

21. Ganim, Z.; Jones, K. C.; Tokmakoff, A., Insulin Dimer Dissociation and Unfolding Revealed by Amide I Two-Dimensional Infrared Spectroscopy. *Phys. Chem. Chem. Phys.* **2010**, *12*, 3579-88.